

# A visco-elasto-plastic softening model and it's application for solving static and dynamic stability problems in potash mining

W. Minkley & W. Menzel

*Institut für Gebirgsmechanik GmbH, Leipzig, Germany*

H. Konietzky & L. te Kamp

*ITASCA Consultants GmbH, Gelsenkirchen, Germany*

**ABSTRACT:** To describe the softening-, dilation and creep behavior of salt rock a new visco-elasto-plastic constitutive model was developed, which is based on a modified Mohr-Coulomb model coupled with a non-linear Burgers creep model. The material model is available as a DLL-application for the codes FLAC, FLAC<sup>3D</sup>, UDEC and 3DEC. The theoretical background as well as practical applications for the solution of static and dynamic stability problems in potash mines are given.

## 1 INTRODUCTION

A new and very complex, but relatively easy to use material model with just a few parameters is presented. The visco-elasto-plastic constitutive model contains primary, secondary and tertiary creep and handles softening including dilation effects.

The paper also presents the practical application of the new constitutive model for the back-analysis of lab-tests, the pillar design up to the calculation of dynamic system stability of room and pillar systems in potash mines. Using this new model, it was possible for the first time to predict a mining induced rock burst.

## 2 VISCO-ELASTIC-PLASTIC MATERIAL MODEL

A constitutive model for the description of the softening and dilation behavior of salt rock should have the following characteristics:

- non-linear failure envelope depending on the minimum principle stress,
- deformation- and stress depending softening,
- dominant plastic flow without softening under high confinement,
- dilation depends strongly on the confinement.

A failure criterion which satisfies the above mentioned demands on the basis of a modification of the Mohr-Coulomb model was developed by Minkley (1997):

$$\mathbf{s}_{1B} = \mathbf{s}_D + N_f \cdot \mathbf{s}_3 \quad (1)$$

The function for the friction angle is shown in Figure 1:

$$N_f = 1 + \frac{\mathbf{s}_{MAX} - \mathbf{s}_D}{\mathbf{s}_f + \mathbf{s}_3} \quad (2)$$

$$\mathbf{s}_{eff,B} = \mathbf{s}_D + \frac{\mathbf{s}_{MAX} - \mathbf{s}_D}{\mathbf{s}_f + \mathbf{s}_3} \cdot \mathbf{s}_3 \quad (3)$$

where  $\sigma_3$  = minimum principal stress,  $\sigma_{1B}$  = maximum principal stress at failure,  $\sigma_{eff,B} = \sigma_{1B} - \sigma_3$  = maximum effective stress,  $\sigma_D(\epsilon^P)$  = uniaxial compressive strength,  $\sigma_{MAX}(\epsilon^P)$  = maximum effective strength,  $\sigma_\Phi(\epsilon^P)$  = curvature parameter for strength surface,  $\epsilon^P$  = plastic shear deformation.

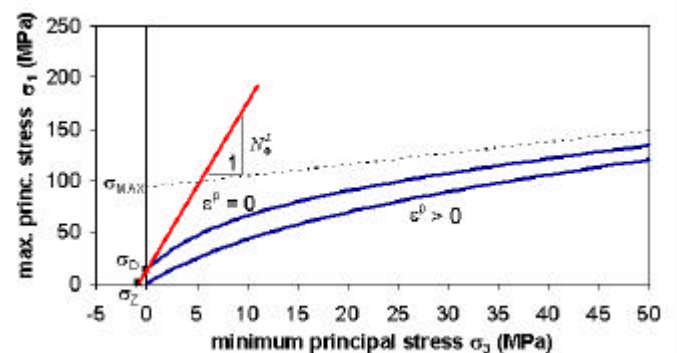


Figure 1. Linear and non-linear Mohr-Coulomb failure criteria

Equation 2 can also be written as:

$$N_f = 1 + \frac{1}{\frac{1}{N_f^L - 1} + \frac{\mathbf{s}_3}{\mathbf{s}_{MAX} - \mathbf{s}_D}} \quad (3)$$

where  $N_\phi^L$  is the well-known friction angle relation of the non-linear Mohr-Coulomb failure criterion, which do not depend on stresses. For  $\sigma_3=0$ , it follows that:

$$N_\phi = N_\phi^L = \frac{1 + \sin\phi}{1 - \sin\phi} \quad (4)$$

The non-linear failure criterion contains only one additional parameter  $\sigma_{MAX}$ . The physical meaning of  $\sigma_{MAX}$  becomes clear, if the failure criterion is plotted as  $\sigma_1 - \sigma_3 = f(\sigma_3)$ .  $\sigma_{MAX}$  is the maximum effective stress the rock can carry and to which the failure criterion moves towards with increasing minimum principal stress  $\sigma_3$ . For rock salt under mining conditions the non-linearity of the failure envelope can not be ignored. It follows from (4):

$\sigma_{MAX} \rightarrow \infty$ :  $N_\phi = N_\phi^L$ , i.e., under the assumption of an unlimited maximum effective strength, the modified non-linear Mohr-Coulomb model passes into the classical Mohr-Coulomb model. The non-linear failure criterion describes both, compression as well as tension. More precisely, the tensile strength is given by:

$$\sigma_z = \frac{1}{2} \cdot (\sigma_\phi + \sigma_{MAX}) - \sqrt{\frac{1}{4} (\sigma_\phi + \sigma_{MAX})^2 - \sigma_D \cdot \sigma_\phi} \quad (5)$$

Approximately is valid:

$$\sigma_z \approx \frac{\sigma_D}{\sigma_{MAX}} \cdot \sigma_\phi \quad (6)$$

The compressive strength  $\sigma_D$ , the tensile strength  $\sigma_z$ , the maximum effective strength  $\sigma_{MAX}$  and the curvature parameter  $\sigma_\phi$  are related by:

$$s_f = \frac{s_{MAX} - s_z}{\frac{s_D - 1}{s_z}} \quad (7)$$

$$s_f = \frac{s_{MAX} - s_D}{N_f^L - 1} \quad (8)$$

From the modified non-linear Mohr-Coulomb failure criterion (1), the flow rule can be deduced (pressure with negative sign):

$$f_s = \sigma_1 - \sigma_3 + \sigma_D - \frac{\sigma_{MAX} - \sigma_D}{\sigma_\phi - \sigma_3} \cdot \sigma_3 \quad (9)$$

The plastic potential for non-associated flow is given by:

$$g_s = \sigma_1 - \sigma_3 - \frac{\sigma_{MAX, \psi} - \sigma_D}{\sigma_\psi - \sigma_3} \cdot \sigma_3 \quad (10)$$

If the failure envelope is reached, plastic deformations occur in addition to the elastic deformations. Using the flow rule, the plastic incremental deformation part can be determined:

$$\Delta \varepsilon_i^P = \lambda_s^* \cdot \frac{\partial g_s}{\partial \sigma_i} \quad i = 1, 3 \quad (11)$$

Besides the elasto-plastic characteristics most of the salt rocks show viscous behaviour. Therefore, the elasto-plastic softening model is combined with the Burgers creep model. The incremental form of the Burgers model is given in the FLAC manuals (ITASCA, 1998). The determination of the multiplier  $\lambda_s^*$  in (11) is obtained for  $f_s=0$ :

$$\lambda_s^* = \frac{\sqrt{C_4^*} - C_2^*}{2 \cdot C_1^*} \quad (12)$$

$$C_1^* = -\frac{1}{s_f} (a_2 - a_1 \cdot N_\psi) \cdot [(a_2 - a_1 \cdot N_\psi) - (a_1 - a_2 \cdot N_\psi)]$$

$$C_2^* = -\frac{1}{\sigma_\phi} (\alpha_2 - \alpha_1 \cdot N_\psi) \cdot (\sigma_1 - 2 \cdot \sigma_3 + \sigma_{MAX} + \sigma_\phi) + (\alpha_1 - \alpha_2 \cdot N_\psi) \cdot \left(1 - \frac{\sigma_3}{\sigma_\phi}\right)$$

$$C_3^* = \frac{\sigma_3}{\sigma_\phi} \cdot (\sigma_1 - \sigma_3 + \sigma_{MAX}) - (\sigma_1 - \sigma_3 + \sigma_D)$$

$$C_4^* = C_2^{*2} - 4 \cdot C_1^* \cdot C_3^*$$

$$\alpha_1 = K + \frac{2}{3 \cdot a} \quad \alpha_2 = K - \frac{1}{3 \cdot a}$$

$$a = \frac{1}{2 \cdot G^M} + \frac{\Delta t}{4} \cdot \left( \frac{1}{\eta^M} + \frac{1}{A^* \cdot \eta^K} \right)$$

$$A^* = 1 + \frac{G^K \cdot \Delta t}{2 \cdot \eta^K}$$

$N_\psi$  is the dilation function:

$$N_\psi = 1 + \sigma_\psi \frac{(\sigma_{MAX, \psi} - \sigma_D)}{(\sigma_\psi - \sigma_3)^2} \quad (13)$$

For volume increase (dilation) is valid:

$$\frac{\Delta V}{V_0} = \varepsilon_{VOL}^P = (N_\psi - 1) \cdot \varepsilon_1^P \quad (14)$$

For  $\sigma_3 = 0$ , from the (13) and (14) follows:

$$\frac{\varepsilon_{VOL,0}^P}{\varepsilon_1^P} = \frac{\sigma_{MAX, \psi} - \sigma_D}{\sigma_\psi} \quad (15)$$

where

$$\frac{\varepsilon_{VOL,0}^P}{\varepsilon_1^P} = \tan \beta^0$$

is the slope of the volume deformation curve (Figure 4b)  $\varepsilon_{VOL}^P = f(\varepsilon_1^P)$  in the dilation area under uniaxial load ( $\sigma_3=0$ ). Therefore, the dilation function can be written as:

$$N_\psi = 1 + \frac{\sigma_\psi^2}{(\sigma_\psi - \sigma_3)^2} \cdot \tan \beta^0 \quad (16)$$

where  $\tan(\beta^0)$  and  $\sigma_\psi$  depend on the plastic deformation  $\varepsilon_1^P$ . If the curvature parameter of the dilatancy function moves, so that  $\sigma_\psi \rightarrow \infty$ , a linear relation yields:

$$N_\psi^L = 1 + \tan \beta \quad (17)$$

with the common description of the dilation with constant stress-independent dilation angle:

$$\psi = \arcsin\left(\frac{\tan \beta}{2 + \tan \beta}\right) \quad (18)$$

The elastic constants (shear modulus  $G$  and in analogy the bulk modulus  $K$ ) are given by an empirical relation:

$$G = G_R + \frac{1}{1 + f \cdot \varepsilon_{VOL}^P} \cdot G_0 \quad (19)$$

where

- $G_0 = G - G_R$
- $G$  - shear modulus of intact rock
- $G_R$  - shear modulus of rock in the post-failure region
- $f$  - material parameter.

The new model is able to describe the creep behavior including creep rupture. The primary creep phase is modeled by the Kelvin-Model with Kelvin shear modulus  $G^K$  and Kelvin viscosity  $\eta^K$ . The secondary creep phase is controlled by the Maxwell viscosity  $\eta_M$ . The tertiary creep phase is governed by a dilation softening mechanism. Under the assumption  $\eta^K \rightarrow \infty$  and  $\eta^M \rightarrow \infty$ , (12) yields  $a = \frac{1}{2G^M}$  and the material model coincides with the time-independent elasto-plastic model. Within the visco-elasto-plastic material model, the stress dependency of the creep rate is governed by the exponential dependency of the Maxwell viscosity on the deviatoric stress  $\sigma_V$  (Lux, 1984):

$$\eta^M = \eta_0^M \cdot e^{m \cdot \sigma_V} \quad (20)$$

## 2 SIMULATION OF UNIAXIAL AND TRIAXIAL COMPRESSION TESTS

The numerical simulation of lab tests is based on experiments on carnallitic samples (Figure 2 and 3). Both, the lab and numerical samples have a height to width ratio of 2 to 1. Between the end platens and the sample, a friction angle of 15 degree was assumed. The axial load was applied under constant deformation velocity and the confining pressure was kept constant (servo-controlled test). The calculation of the volume change starts after isotropic consolidation.

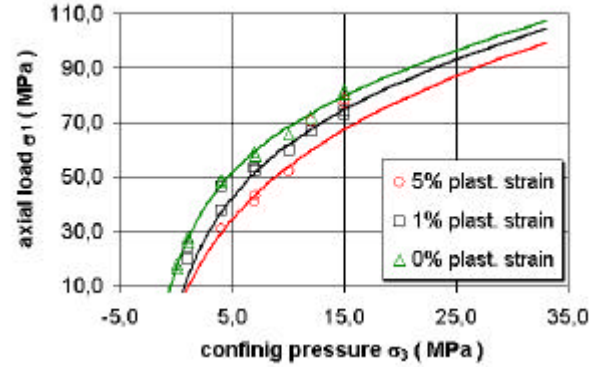


Figure 2. Measured and calculated failure envelope for  $C_{60}$ .

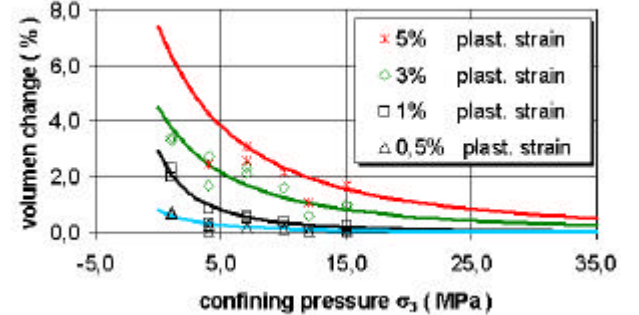


Figure 3. Measured and calculated dilatancy behaviour of  $C_{60}$ .

Until the peak strength is reached a linear stress-strain relation is assumed (Figure 4a). After the peak strength has been reached, dilation softening takes place and the load bearing capacity decreases until the total loss of the bearing capacity is observed. The softening modulus, which determines the steepness of the load bearing capacity reduction in the post-failure region, decreases with increasing confinement as observed in the lab. First, the calculated volume change shows a linear compaction determined by the elastic constants  $E$  and  $\nu$  followed by the plastification with volume increase, which is caused by micromechanical damage (micro-cracks). In agreement with the lab tests, the numerical model shows a strong dependence of the dilatation on the confining pressure (Figure 4b). Also, the flattening of the  $\varepsilon_V = f(\varepsilon_1)$ -curve in the post-failure region, caused by macroscopic rupture planes, is reproduced by the model due to the dilatation function (equation 16).

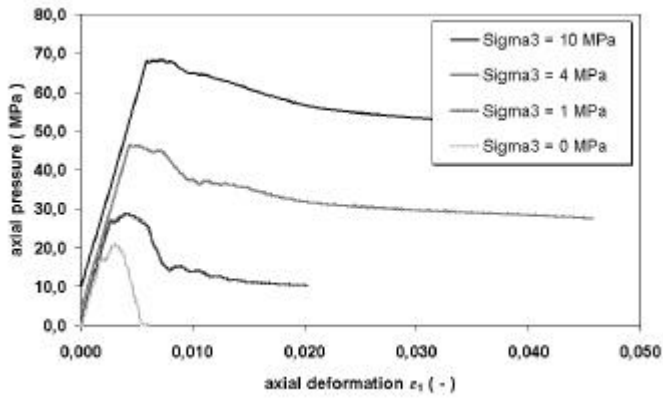


Figure 4a. Triaxial stress-strain curves for C<sub>60</sub>.

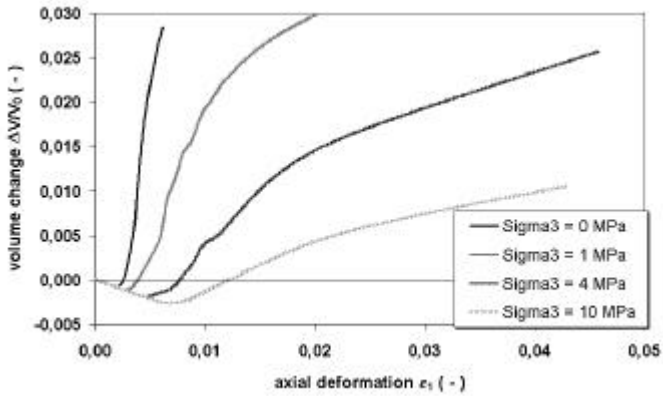


Figure 4b. Volume change versus axial deformation for C<sub>60</sub>.

Figure 5 shows the results of uniaxial compressive creep tests (Table 1). After reaching 85% of the compressive strength, damage caused dilation (volume increase) is observed (Figure 5). After 150 days of creep, dilation increases strongly and after app. 1 year of creep failure takes place.

Table 1. Material parameters for the carnallitic rock C<sub>60</sub>.

$G^M$	$K^M$	$\eta^M$	$m$	$G^K$
GPa	GPa	MPa*d	MPa <sup>-1</sup>	GPa
4	6,7	$4 \cdot 10^{-6}$	0,17	2

$\eta^K$	$\sigma_D$	$\sigma_{MAX}$	$\sigma_\phi$
MPa*d	MPa	MPa	MPa
$1 \cdot 10^4$	8 <sup>1)</sup>	86 <sup>1)</sup>	25 <sup>1)</sup>

<sup>1)</sup> failure surface = dilatancy surface

If the initial load is smaller and therefore the initial damage is reduced, the axial deformation and the creep time increases until the creep rupture occurs. If the load is so small, that creep without dilation takes place, creep rupture does not occur.

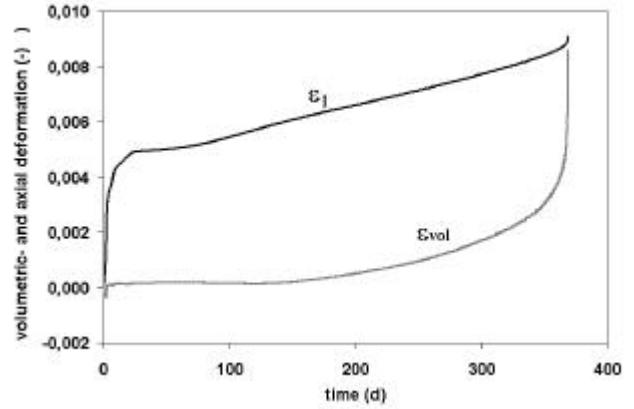


Figure 5. Deformation versus time for C<sub>60</sub> during an uniaxial compression test.

### 3 BRITTLE FAILURE OF CARNALLITIC PILLARS

The deformation and failure behavior of potash mines depends on the long-term stability of the load bearing elements (Minkley & Menzel, 1996). The contour damage due to the nearly uniaxial loading is of greatest importance for the fracture process of carnallitic pillars.

The contour damage of carnallitic pillars was modeled with 3DEC. The pillar models consist of a 6 m thick carnallitic layer embedded in two 6 m thick salt layers. Within a parameter study, the influence of the ratio between pillar width and height as well as different pillar depths were investigated in respect to the load bearing capacity. The upper and lower model boundaries were moved against each other with a resultant velocity of 1 m/s, which is a typical value for an excitation during mine bursts in carnallitic room and pillar systems. For the calculations the softening parameters given in Table 2 were used.

Table 2. Plastic material properties (failure envelope) for the pillar model.

Layer	Compressive strength $\sigma_D$ [MPa]	Max. effective strength $\sigma_{MAX}$ [MPa]	Curvature parameter $\sigma_\phi$ ( $\epsilon^P$ )
Halite	35	66	4
Carnallite C <sub>60</sub>	17,2	86	6,7

The behavior of the pillar models depend on the ratio between pillar width and height, the contact conditions between the pillar and the adjacent rock, the dilation of the pillar rock and on the cross section geometry of the pillars (quadratic or elongated). For long pillars with a width to height ratio of 4, the contour damage does not reach the pillar core and the pillar does not lose its load bearing capacity if dilation is taken into account. On the other side, the quadratic pillars with the same height to width ratio show complete failure. In both cases the contact condition was: friction angle of 15 degree and zero cohesion. Under static loading, cohesion has been assumed besides the contact friction. Under dynamic

loads, contact cohesion and the static friction can be lost completely, otherwise mining bursts in carnalitic mines would not have occurred (Minkley, 1989). Long pillars with a width to height ratio of 6 show a penetration of the pillar into the over- and under-lying strata. Only minor softening is observed (Figure 6 and 6a). Under the action of dilatation, even hardening can be observed.

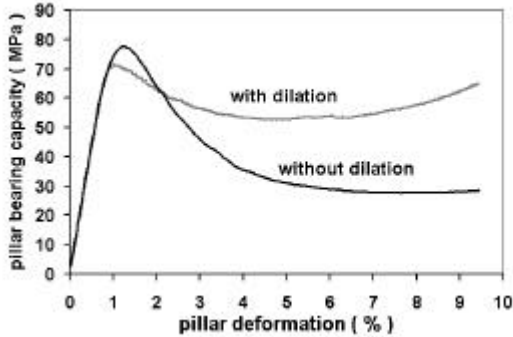


Figure 6. Pillar bearing capacity of long pillars with and without consideration of dilatation.

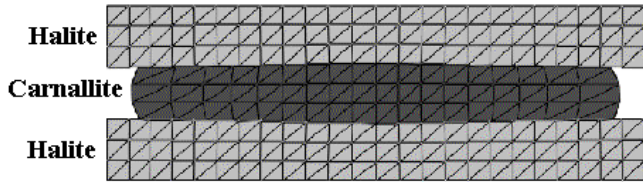


Figure 6a. Pillar model with grid structure (coarse mesh).

Using very fine meshes, the damage mechanism including localization (shear band development) can be observed with the new model. The grid for the calculations performed with UDEC (long pillar with a width to height ratio of 4), shown in Figure 7, has a gridpoint distance of only 0.2 m. This pillar, which consists of C<sub>60</sub>, has a maximum load bearing capacity of 48 MPa and was loaded with 32 MPa (Figure 7). The Figure shows the development of shear bands and the area of dilatation. Within the shear bands the volume increase reaches 10% and has led to significant damage. If one assumes, that areas with values of dilatation greater 1% fall out of the pillar contour, a concave shaped pillar develops (Figure 7, right) as observed in nature (Figure 8).



Figure 7. Dilatation development (left) and corresponding fall-out (right).



Figure 8: Typical pillar contour damage.

Another example, modeled with FLAC, demonstrates the effect of pillar robbing. The width to height ratio was reduced from 4.2 to finally 2.9. During the pillar cross section reduction from 4.2 to 3.3 primary and secondary creep is observed, but further reduction of the cross section leads finally to creep rupture (Figure 9).

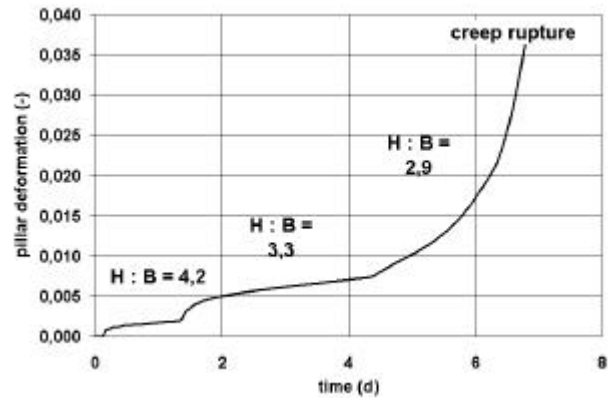


Figure 9. Pillar deformation versus time as a function of cross section reduction.

#### 4 CALCULATIONS OF MINING BURSTS IN POTASH MINES

Several geomechanical investigations are available about the last big potash mining tremor, which has taken place in Teutschenthal 1996, including a prediction with FLAC one month before the burst occurred (Arge, 1996).

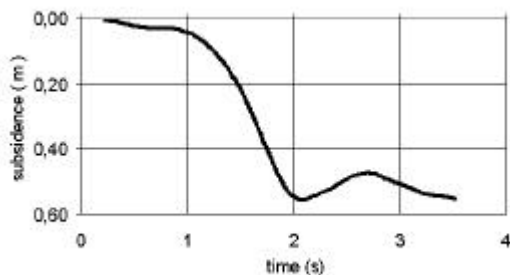


Figure 10. Calculated surface movement versus time during the Teutschenthal rock burst.

During that rock burst, 700 long pillars were destroyed in a chain-like reaction, so that a mine field with an area of 2.5 km<sup>2</sup> in 620 m to 770 m depth collapsed.

A comparison between the numerical prediction and the in situ investigations gave the following results (Minkley & Menzel, 1999):

- the predicted time scale for the source mechanism of 1.5 s and the vibrations of the overlying strata after 2 s (Figure 10) are in agreement with the seismological investigations,
- the fracture process was stopped by the 110 m wide barrier pillar as predicted by the model,
- the predicted magnitude of 5 agrees well with the average measured magnitude of 4.8,
- the predicted maximum surface subsidence of 0.5 m was confirmed by the measurements,
- the predicted intensity was one degree above the intensity value, deduced by the evaluation of the damage at the surface.

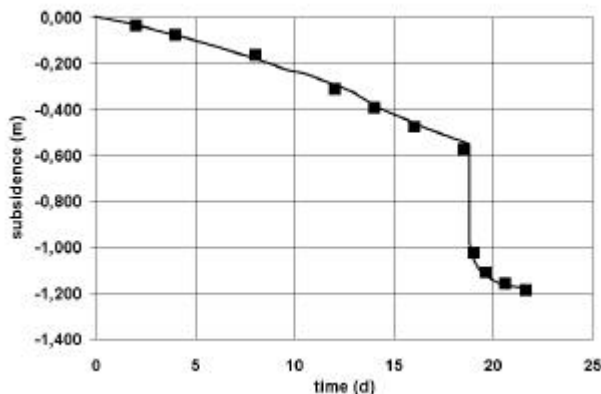


Figure 11. Measured and calculated surface subsidences.

After the rock burst visco-elasto-plastic calculations were performed to understand why the room-and-pillar system could have been collapsed without external dynamic input, like observed during the Teutschenthal rock burst in 1996. The visco-elasto-plastic back-analysis included the gradual creation of rooms over 14 years. The measured surface subsidences were used for the model calibration (Figure 11). Within preliminary elasto-plastic calculations, a dynamic excitation was created by a sudden reduction of the pillar width of two pillars by 4 m each. This dynamic excitation leads to pillar collapse and subsequent collapse of the whole system. During this short dynamic phase, the viscous behavior of the salt rocks is inactive and the material behaves brittle. Only a few years after the rock burst with decreasing creep rates, the material reaches the stationary creep phase.

Instead of using an external dynamic input to model the burst, the new visco-elasto-plastic approach allows to model the burst by creep rupture (time-dependent softening). If due to the time-dependent pillar contour strength reduction the bearing capacity of the pillar is reached, accelerating creep and finally

system instability is observed. The calculated subsidence development at the surface (Figure 12a) and the 2<sup>nd</sup> stopping level (Figure 12b) is in excellent agreement with the measurements.

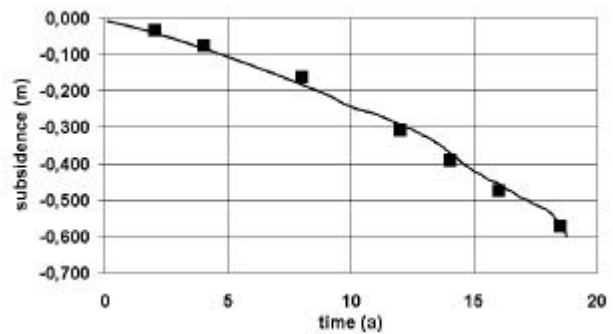


Figure 12a: Measured and calculated surface subsidences.

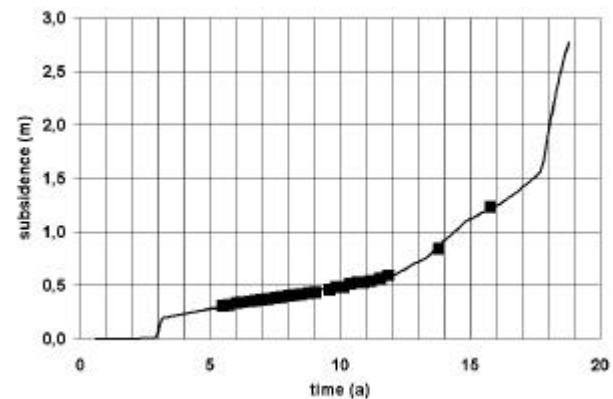


Figure 12b. Measured and calculated subsidences at the 2<sup>nd</sup> stopping level.

On the basis of the new visco-elasto-plastic constitutive law a self-contained model about the mechanism of the Teutschenthal mine burst was established, which contains the following elements: initialization of brittle failure by creep rupture, chain-reaction of pillar collapses, corresponding energy radiation and subsequent damage of the surrounding rock mass.

## 5 CONCLUSIONS

The new visco-elasto-plastic constitutive law which includes stress- and deformation dependent softening and dilation considers the non-linear behavior of salt rocks and allows a much more precise modeling of the deformation depending damage up to the brittle failure.

The combination of the developed softening law with the modified Burgers-creep law allows to analyze time-depending softening processes with transient, stationary and tertiary creep up to the final creep rupture.

The developed law can be used by FLAC, FLAC<sup>3D</sup>, UDEC and 3DEC via the DLL-technique.

The development of the constitutive law was governed by the interaction between theory, experiment and practical application. Although the constitutive law inhibits a quite complex material behavior, the

law is characterised by only a few parameters, which can be determined by conventional servo-controlled uniaxial and triaxial lab tests with measuring the volume change.

For the verification of the constitutive law several lab tests were back-analyzed, which include the phenomena of localization, reduction of the softening and dilation with increasing confinement, time-dependent softening and creep rupture.

The back-analysis of the mine burst in Teutschenthal in 1996 can be considered as a comprehensive validation.

## 6 ACKNOWLEDGEMENT

The work was supported by the BMBF of Germany under the registration number 02-C-0264. The authors are responsibly for the content of the paper.

## REFERENCES

- Arge 1996 (IfG Leipzig, ERCOSPLAN Erfurt, K-UTEC Sonderhausen & Schwandt, A.).  
*Bewertung der Langzeitsicherheit Grube Teutschenthal der GTS GmbH & Co. KG.* IfG Leipzig, 9. August 1996, unveröffentlicht
- ITASCA 1998. FLAC-Manual.  
ITASCA Consulting Group, Inc. Minneapolis, Minnesota, USA.
- Minkley, W. & Menzel, W. 1996. Dynamic system stability of mining structures in salt mining *Proc. 2<sup>nd</sup> North America Rock Mechanics Symposium. NARMS'96*, Montreal, Vol. 1, 93-100, June 19-21.
- Minkley, W. 1997. Spröbruchverhalten von Carnallit und seine Auswirkungen auf die Langzeitsicherheit von Untertagedeponien. Forschungszentrum Karlsruhe GmbH, *Wissenschaftliche Berichte FZKA-PTE-Nr. 5*, 249 – 275.
- Minkley, W. 1989. Festigkeitsverhalten von Sedimentgesteinen im Post-failure-Bereich und Gebirgsschlagerscheinungen. *Proc. Int. Symp. Rock at Great Depth*, Pau, Vol. 1, 59 – 65.
- Minkley, W. & Menzel, W. 1999. Vorausberechnung des Kollapses eines Grubenfeldes - Gebirgsschlag Teutschenthal 11. September 1996. *Proc. 9<sup>th</sup> Int. Congress on Rock Mechanics*, Paris, Vol. 2, 1115 – 1118.
- Lux, K.-H. 1984. *Gebirgsmechanischer Entwurf und Felderfahrungen im Salzkavernenbau.*  
F. Enke Verlag, Stuttgart.